

# Coarse graining the state space of a turbulent flow using periodic orbits

Gökhan Yalnız,<sup>1,2</sup> Björn Hof,<sup>1</sup> and Nazmi Burak Budanur<sup>1</sup>

<sup>1</sup>*IST Austria, 3400 Klosterneuburg, Austria*

<sup>2</sup>*Physics Department, Boğaziçi University, 34342 Istanbul, Turkey*

(Dated: October 11, 2024)

We show that turbulent dynamics that arise in simulations of the three-dimensional Navier–Stokes equations in a triply-periodic domain under sinusoidal forcing can be described as transient visits to the neighborhoods of unstable time-periodic solutions. Based on this description, we reduce the system with more than  $10^5$  degrees of freedom to an 18-node Markov chain where each node corresponds to the neighborhood of a periodic orbit. The model accurately reproduces long-term averages of the system’s observables as weighted sums over the periodic orbits.

Producing low-dimensional models of turbulent flows has been a long-standing scientific challenge with a wide potential for applications. Following the discoveries [1–6] of unstable time-invariant solutions (equilibria, traveling waves, periodic orbits, ...) of three-dimensional (3D) fluid flows in pipes and channels, Gibson *et al.* [7] demonstrated the influence of invariant solutions on the dynamics of plane Couette flow through state space visualizations. Although the underlying hypothesis that such solutions could be eventually used for turbulence modeling has been further discussed and elaborated in subsequent studies [8–11], a clear path towards this goal remained missing.

The studies of invariant solutions of turbulent flows are founded upon a view of fluid dynamics as a high-dimensional dynamical system [12]. In a computational setting, such a dynamical system is constructed by a spatial discretization that yields a numerical representation of the fluid’s state and a simulator that sets the time-evolution rule. The simplest invariant solutions of continuous-time dynamical systems are equilibria, which in fluid dynamics correspond to velocity fields that are stationary. Even though equilibria can influence chaotic flows through their stable and unstable manifolds [7, 13], they by definition lack dynamics and on their own cannot be used for modeling. At the focus of the present work are periodic orbits, which form loops in the state space and correspond to velocity fields that recur exactly after a constant period.

Unstable periodic orbits that are embedded in strange attractors offer a systematic way of exploring chaos since the periodic orbits and the chaotic trajectories in their vicinity have similar physical properties [14]. However, the instability of periodic orbits necessitates special techniques for their numerical discovery and poses a technical challenge especially in high-dimensional settings such as shear flow simulations. Nevertheless, extensive searches for periodic orbits in high-dimensional systems became possible after Viswanath’s introduction of the Newton–Krylov–hookstep algorithm [15]. Since then, a large number of periodic orbits were computed in plane Couette [8] and pipe [10] flows where similarities between turbulent flows and periodic solutions were observed. However, in these studies no attempt was made to construct a turbu-

lence model based on periodic orbits.

In this Letter, we present a quantitatively accurate reduced-order model of a 3D shear flow based on the numerically computed periodic solutions of the governing equations. Specifically, we consider 3D Kolmogorov flow [16] under certain symmetry restrictions and utilize the recently-introduced [17] state space persistence analysis for quantifying similarities between turbulence and periodic orbits to show that the transitional turbulence in this system can be decomposed into consecutive visits to the neighborhoods of the periodic orbits. Consequently, we propose the neighborhoods of periodic orbits as the bases of a Markov process that serves as a coarse-grained model of the turbulent flow. Upon comparing the long-term observable averages from numerical simulations to those obtained from the invariant measure of the Markov chain, we show that the periodic orbits give an approximation to the natural measure [18–20] of the system.

3D Kolmogorov flow is described by the body-forced Navier–Stokes equations

$$\mathbf{u}_t + \mathbf{u} \cdot \nabla \mathbf{u} = -\nabla p + \nu \nabla^2 \mathbf{u} + \mathbf{f} \quad (1)$$

in a rectangular box  $[0, L_x] \times [0, L_y] \times [0, L_z]$ , where  $\mathbf{u} = [u, v, w](x, y, z)$  and  $p = p(x, y, z)$  are the velocity and pressure fields respectively,  $\nu$  is the kinematic viscosity,  $\mathbf{f} = \sin(2\pi y/L_y)\hat{\mathbf{e}}_x$  is the forcing term, and  $\hat{\mathbf{e}}_x$  denotes the unit vector in  $x$  direction. The velocity field  $\mathbf{u}$  satisfies the incompressibility condition  $\nabla \cdot \mathbf{u} = 0$  and periodic boundary conditions in all three directions. The volume-integrated quantities of interest are the total kinetic energy  $E = \frac{1}{2} \int \mathbf{u} \cdot \mathbf{u} \, d\mathbf{x}$ , and the instantaneous rates of energy input  $I = \int \mathbf{u} \cdot \mathbf{f} \, d\mathbf{x}$  and dissipation  $D = \nu \int \boldsymbol{\omega} \cdot \boldsymbol{\omega} \, d\mathbf{x}$ , where  $\dot{E} = I - D$  and  $\boldsymbol{\omega} = \nabla \times \mathbf{u}$  is the vorticity. The laminar solution of (1) is given by  $u_L = \nu^{-1} \sin(2\pi y/L_y)$ ,  $v_L = 0$ ,  $w_L = 0$  and it is linearly stable for all  $\nu$  [21]. Despite the linear stability of  $\mathbf{u}_L$ , turbulence in this system can be triggered by finite-amplitude perturbations and is transient at high  $\nu$  [21]. In this sense, 3D Kolmogorov flow admits the basic phenomenology of the transitional turbulence in wall-bounded shear flows such as those in pipes and channels [22].

For numerical integration of (1), we developed a pseudospectral [23, 24] solver based on the open-source `hit3d`

code [25]. We adapted the Newton-Krylov-hookstep implementation of `Openpipeflow` [26] for finding periodic orbits numerically and utilized `scikit-tda` [27] for topological data analysis. In all of our results to follow, the kinematic viscosity is set to  $\nu = 0.05$ , the size of our computational domain is  $L_x \times L_y \times L_z = 2\pi \times 2\pi \times \pi$ , the numbers of spatial grid points are  $[N_x, N_y, N_z] = [64, 64, 32]$ , and the second-order predictor-corrector time step is set to  $\Delta t = 0.0025$ . Fourier-expanded fields are dealiased following the 2/3 rule and the nonzero Fourier coefficients show at least four orders of magnitude drop off at all times in each direction. The number of nonzero Fourier coefficients after dealiasing is 108320.

3D Kolmogorov flow is equivariant under the continuous translations  $T_x(\delta x)$  and  $T_z(\delta z)$  in  $x$  and  $z$  directions by  $\delta x$  and  $\delta z$ , respectively, and the discrete symmetries [21]

$$R_{xy}[u, v, w](x, y, z) = [-u, -v, w](-x, -y, z), \quad (2)$$

$$R_y[u, v, w](x, y, z) = [u, -v, w](x, -y - L_y/2, z), \quad (3)$$

$$R_z[u, v, w](x, y, z) = [u, v, -w](x, y, -z), \quad (4)$$

$$S_x[u, v, w](x, y, z) = [-u, v, w](-x, y - L_y/2, z). \quad (5)$$

As a simplification, we restrict our study to the flow-invariant subspace of the velocity fields that are symmetric under  $S_x$  and  $R_z$ . While this choice avoids complications due to the continuous symmetries [28] by allowing for translations only by  $L_x/2$  and  $L_z/2$  in  $x$  and  $z$  directions respectively, this flow-invariant subspace still exhibits transient turbulence with lifetimes of  $O(1000)$ , which is more than 300 times the period of our shortest periodic orbit. Since invariance under  $S_x$  equates the action of  $R_{xy}$  and  $R_y$ , denoting identity element with  $I$  we can write the symmetry group of the system as

$$G = \{I, T_{x/2}, T_{z/2}, R_{xy}, T_{x/2} T_{z/2}, T_{z/2} R_{xy}, T_{x/2} R_{xy}, T_{x/2} T_{z/2} R_{xy}\}, \quad (6)$$

where  $T_{x/2} = T_x(L_x/2)$  and  $T_{z/2} = T_z(L_z/2)$ .

The presence of symmetries (6) implies that each generic state of the system has 7 symmetry copies that can be generated by the elements of (6). Since our analyses require parsing very large data sets, it is crucial for us to eliminate all redundancies in the data. With this in mind, we construct a symmetry-reduced representation of our system by means of a state space coordinate transformation. Let  $\xi$  be a state vector holding the real and imaginary parts of coefficients in the Fourier expansion of  $\mathbf{u}$ . Noting that each element of (6) is its own inverse, we decompose  $\xi$  into symmetric and antisymmetric components under the action of  $\sigma \in G$  as  $\tilde{\xi}_\sigma^\pm = \frac{1}{\sqrt{2}}(I \pm \sigma)\xi$ . By construction under the action of  $\sigma$ , the elements of  $\tilde{\xi}_\sigma^+$  are left invariant and those of  $\tilde{\xi}_\sigma^-$  change their signs. Let  $(\rho_1, \rho_2, \rho_3, \rho_4, \dots)$  be the elements of  $\tilde{\xi}_\sigma^-$ , we write the invariants of  $\sigma$  as

$$\left\{ \frac{\rho_1^2 - \rho_2^2}{\sqrt{\rho_1^2 + \rho_2^2}}, \frac{\rho_1 \rho_2}{\sqrt{\rho_1^2 + \rho_2^2}}, \frac{\rho_2 \rho_3}{\sqrt{\rho_2^2 + \rho_3^2}}, \frac{\rho_3 \rho_4}{\sqrt{\rho_3^2 + \rho_4^2}}, \dots \right\}. \quad (7)$$

These invariants, without the denominators, were written for a Fourier-space representation of the Kuramoto–Sivashinsky system in ref. [29]. Here, we introduce the denominators in order to prevent the transformation from producing numbers that are too large or small. One can confirm by inspection that the elements of (7) are invariant when all  $\rho_i$  change their signs but not when any other subset of  $\rho_i$  does. Thus, replacing the elements of  $\tilde{\xi}_\sigma^-$  with (7) gives us coordinates that are invariant under  $\sigma$ . We begin this procedure with the reduction of  $T_x(L_x/2)$ , and repeat for  $T_z(L_z/2)$  and  $R_{xy}$  in order to obtain the symmetry-reducing 8-to-1 coordinate transformation. Hereafter unless stated otherwise, we use the symmetry-reduced state space coordinates  $\xi$  and the  $L_2$  inner product  $\langle \xi^{(k)}, \xi^{(l)} \rangle = \sum_i \xi_i^{(k)} \xi_i^{(l)}$  in our computations.

At the first stage of our study, similar to refs. [8, 10], we generated turbulent data sets from random initial conditions and searched for periodic orbits starting from near-recurrences of the turbulent flow as measured by  $R(t, t') = \|\mathbf{u}(t+t') - \mathbf{u}(t)\| / \|\mathbf{u}(t)\|$ , where  $\|\cdot\|$  denotes the  $L_2$  norm. This process resulted in 18 distinct periodic orbits with relative errors  $\|\mathbf{u}_p(t+T_p) - \mathbf{u}_p(t)\| / \|\mathbf{u}_p(t)\|$  less than  $10^{-9}$ . Hereafter, we refer to these orbits as  $\bar{\rho}o_i$  with indices  $i = 1, 2, \dots, 18$  ordered in increasing periods, where the shortest period  $T_1 = 2.807$  and the longest one  $T_{18} = 17.3382$  [30]. The periodic orbits along with a long dataset sampled from turbulent trajectories are shown in Fig. 1 (a) on the  $ID$  plane, axes of which correspond to the instantaneous rates of energy input and dissipation. A different visualization of the periodic orbits and turbulence is given in Fig. 1 (b), where we projected them onto the leading three principal components [31] that are obtained from 444 uncorrelated turbulent samples in the symmetry-reduced state space.

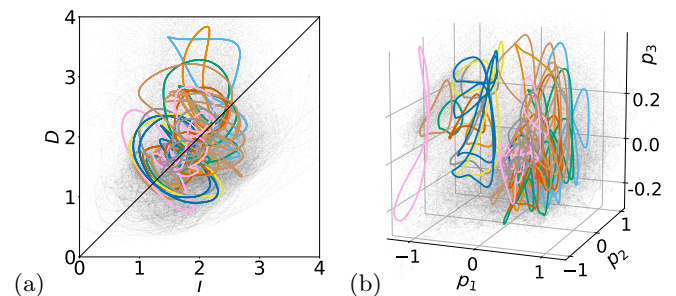


FIG. 1. (Color online) Turbulent trajectories (dots, gray) and periodic orbits (loops, colors) visualized (a) on the  $ID$  plane, and (b) as projections onto the three leading principal components.

The first question that we address in the following is how frequently individual periodic orbits are visited, i.e. *shadowed*, by the turbulent flow. We achieve this by state space persistence analysis which we summarize next and refer the reader to ref. [17] for details. Our analysis begins with producing projection bases that locally capture periodic orbits. To this end, we take snapshots along one

period of each orbit with the sampling time  $t_s = 0.1$  and generate the associated principal components. Next, we simulate turbulent flow and project it onto each of these bases centered at the empirical mean of the respective periodic orbit. As an illustration, Fig. 2 (a) shows  $\overline{p\bar{o}}_{17}$  along with a shadowing turbulent trajectory spanning a time window equal to the period  $T_{17} = 17.01$  of  $\overline{p\bar{o}}_{17}$  as projections onto the leading three principal components of  $\overline{p\bar{o}}_{17}$ . The main idea of state space persistence analysis is quantifying the shape similarity of projections of the periodic orbits and those of turbulent trajectories such as the ones shown in Fig. 2 (a). For this purpose, we utilize persistent homology, which we briefly describe next and refer the interested reader to refs. [32–34] for in-depth introductions to the subject.

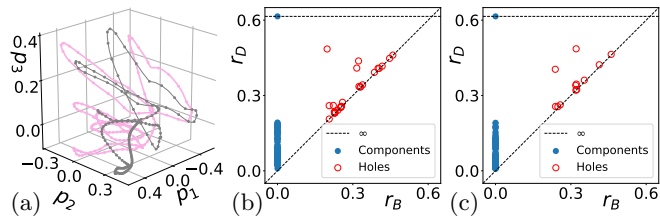


FIG. 2. (Color online) (a) The periodic orbit  $\overline{p\bar{o}}_{17}$  (pink/thick) and a shadowing trajectory (gray/thin) visualized as projections onto the leading three principal components of  $\overline{p\bar{o}}_{17}$ . (b,c) The persistence diagrams associated with  $\overline{p\bar{o}}_{17}$  (b) and shadowing trajectory segment (c) shown in (a). The data points that are used for generating the persistence diagrams (b,c) are marked with dots along the projection curves in (a).

Persistent homology is a computational topology method for extracting shape information from a data set by generating its representations at different resolutions and tracking the topological changes in the process. In our applications, the data sets of interest are the state space projections such as those visualized in Fig. 2 (a) and the final products of the persistence computation are the *persistence diagrams*, examples of which are shown in Fig. 2 (b, c). Each marker in a persistence diagram corresponds to the *birth* and *death* of a topological feature represented by the pair  $(r_B, r_D)$  of birth and death resolutions. For every data set  $\Xi$ , persistent homology gives us two diagrams  $PD_0$  and  $PD_1$  corresponding to the components and holes, respectively [35]. What is gained in this process is a way of quantifying the shape similarity since one can define a metric in the space of persistence diagrams. Assuming each diagram also contains the trivial elements at the diagonal  $r_B = r_D$  with infinite multiplicity, we can define the *bottleneck distance* between  $PD^{(k)}$  and  $PD^{(l)}$  as

$$W_\infty(PD^{(k)}, PD^{(l)}) = \inf_{\phi} \sup_{\mu \in PD^{(k)}} \|\mu - \phi(\mu)\|_\infty, \quad (8)$$

where  $\phi : PD^{(k)} \rightarrow PD^{(l)}$  is a bijection from  $PD^{(k)}$  to  $PD^{(l)}$ . The bottleneck distance (8) can be interpreted as the largest (measured in the  $L_\infty$  norm) of the shortest

one-to-one pairings of the elements of  $PD^{(k)}$  and  $PD^{(l)}$ . With these definitions, we are now in position to define the shadowing distance.

Let  $\Xi^{\overline{p\bar{o}}_i} = \{\hat{\xi}^{\overline{p\bar{o}}_i}(0), \hat{\xi}^{\overline{p\bar{o}}_i}(t_s), \dots, \hat{\xi}^{\overline{p\bar{o}}_i}((N_i-1)t_s)\}$ , and  $\Xi^{(i)}(t) = \{\hat{\xi}(t), \hat{\xi}(t+t_s), \dots, \hat{\xi}(t+(N_i-1)t_s)\}$  be states sampled at rate  $t_s^{-1}$  along one period of  $\overline{p\bar{o}}_i$  and a chaotic trajectory beginning at time  $t$ , respectively, and  $\hat{\cdot}$  denote the projection onto the local bases of  $\overline{p\bar{o}}_i$ . We define the shadowing distance  $S^{(i)}(t)$  of turbulence from  $\overline{p\bar{o}}_i$  at time  $t$  as

$$S^{(i)}(t) = w_0 W_\infty(PD_0^{(i)}(t), PD_0^{\overline{p\bar{o}}_i}) + w_1 W_\infty(PD_1^{(i)}(t), PD_1^{\overline{p\bar{o}}_i}), \quad (9)$$

where,  $PD^{\overline{p\bar{o}}_i}$  and  $PD^{(i)}(t)$  are the persistence diagrams obtained from  $\Xi^{\overline{p\bar{o}}_i}$  and  $\Xi^{(i)}(t)$ , respectively, and  $w_{0,1}$  are the weights of respective contributions from the components and holes. In all of our results to follow, these weights are set to

$$w_{0,1} = [W_\infty(D, PD_0^{\overline{p\bar{o}}_i}) + W_\infty(D, PD_1^{\overline{p\bar{o}}_i})]^{-1}, \quad (10)$$

where  $D$  denotes the empty persistence diagram with diagonal elements only. The choice of the weights (10) sets the shadowing distance of a periodic orbit to an empty data set to 1; thus renders the shadowing distances from different periodic orbits comparable. As an illustration, Fig. 3 (a) shows the shadowing distances of a turbulent trajectory from 9 out of 18 periodic orbits that we found.

We expect the local minima of  $S^i(t)$  to correspond to the episodes of turbulent flow shadowing  $\overline{p\bar{o}}_i$ . Following this assumption, we define the *shadowing decomposition* of a turbulent flow in a time interval  $t \in [t_0, t_f]$  over  $N_{\overline{p\bar{o}}}$  periodic orbits for a threshold distance  $S_{th}$  by the following algorithm. Starting at time  $t = t_0$ , we find  $i_{\min} = \arg \min_i S_i(t)$ . If  $S_{i_{\min}}(t)$  is less than  $S_{th}$ , then we save the pair  $(t, i_{\min})$  and increase  $t$  by the period  $T_{i_{\min}}$  of  $\overline{p\bar{o}}_{i_{\min}}$ ; otherwise, we increase  $t$  by  $t_s$  and repeat the procedure until the final time  $t_f$  is reached. The result of this decomposition is the set of pairs  $(t, i_{\min})$  which we visualized as a bar plot in Fig. 3 (b) for  $S_{th} = 0.5$ . The shadowing decomposition in Fig. 3 (b) corresponds to the same episode as Fig. 3 (a) and the length of each bar is equal to the period of the respective periodic orbit. Supplementary video shows another visualization of this decomposition for  $t \in [0, 100]$  where velocity and vorticity isosurfaces of turbulence are shown next to those of the periodic orbits that are being shadowed along with the local state space projections.

From its shadowing decomposition, we are able to infer a model of the turbulent flow as a Markov chain [36] with the transition matrix  $P$ , whose elements  $P_{ij}$  correspond to the probability of turbulent flow shadowing  $\overline{p\bar{o}}_j$  after  $\overline{p\bar{o}}_i$ . We estimated these probabilities from the shadowing decompositions of 15 different runs with a total run time of  $t_{\text{tot}} = 13827.0$  after discarding the initial transients and the laminarization events. For the threshold choice of  $S_{th} = 0.5$ , we found the shadowing events to

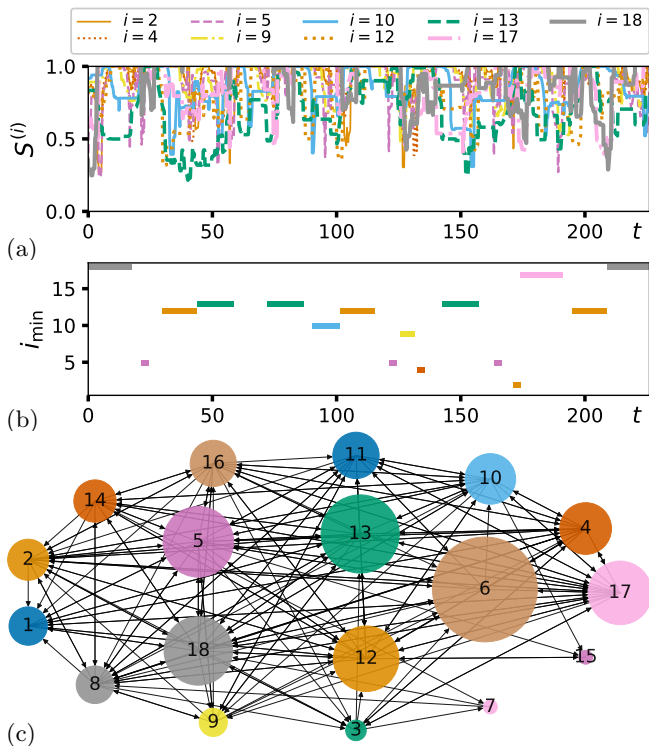


FIG. 3. (Color online) (a) Shadowing distance of a turbulent trajectory from 9 periodic orbits. (b) Shadowing decomposition of the turbulent trajectory. (c) State transition graph where the nodes correspond to periodic orbits and arrows indicate the possible transitions between them. The self-loops are omitted for clarity and the node sizes are proportional to the probability of observing the respective periodic orbit as inferred from the invariant distribution of the corresponding Markov process.

cover 79% of the total time evolution. As a robustness test, we repeated our computations for  $S_{\text{th}} \in [0.4, 0.6]$ . While the fraction of turbulent time evolution that is covered by the periodic orbits differs for different choices of  $S_{\text{th}}$ , it remains always above 50% and the transition probabilities of the Markov process vary only slightly. Therefore, our main results in the following are not sensitive to this threshold choice.

The invariant distribution  $\pi$  of the Markov chain is the left eigenvector of  $P$  with unit eigenvalue, satisfying the normalization condition  $\sum_i \pi_i = 1$ . Fig. 3 (c) shows a network visualization of the Markov chain that models the 3D Kolmogorov flow that we studied here. Each node of Fig. 3 (c) corresponds to a periodic orbit with the size of the node  $i$  proportional to  $\pi_i$  and the directed edges indicate possible transitions from one periodic orbit to the next. In addition to the edges shown in Fig. 3 (c), the nodes have also self-loops (omitted for clarity) that correspond to close recurrence events in which turbulence shadows a periodic orbit for more than a single period. From the invariant distribution  $\pi$ , we can predict long-time averages of the turbulent flow's observables in terms

of their values computed over periodic orbits. Let  $\Omega : \mathcal{M} \rightarrow \mathbb{R}$  be an observable, such as the kinetic energy or dissipation rate, and  $\langle \Omega \rangle_i$  be its average over  $\bar{p} \bar{o}_i$ . The long-time average  $\langle \Omega \rangle$  can be approximated as

$$\langle \Omega \rangle = \frac{\sum_{i=1}^{N_{\bar{p}\bar{o}}} \pi_i T_i \langle \Omega \rangle_i}{\sum_{i=1}^{N_{\bar{p}\bar{o}}} \pi_i T_i}, \quad (11)$$

where we interpret the coefficients  $\pi_i T_i$  as the mean time that chaotic flow spends in the neighborhood of  $\bar{p} \bar{o}_i$ . From (11), we predict the mean kinetic energy and rate of dissipation as  $\langle E \rangle_\pi = 10.76$  and  $\langle D \rangle_\pi = 1.860$ , respectively. These estimates agree with the long-time averages  $\langle E \rangle_\infty = 10.50$  and  $\langle D \rangle_\infty = 1.887$  with 2-digit accuracy, thus, provide with an a posteriori verification of our reduced-order model. We would like to note that the periodic orbit means of the observables can be quite different from the long-time averages with  $\langle E \rangle_i$  and  $\langle D \rangle_i$  taking values as  $\langle E \rangle_i \in \{4.216, 14.269\}$  and  $\langle D \rangle_i \in \{1.326, 2.354\}$  for the periodic orbits that we considered here [30]. It is therefore nontrivial that the weighted sum (11) is in agreement with numerical means.

One feature of the 3D Kolmogorov flow that we do not capture in our model is the laminarization events since we exclude them from our training data. Therefore, the Markov chain and its invariant distribution should be thought of as the model of the nonattracting chaotic set [20] underlying transient turbulence and the natural measure over it, respectively. We would like to note that the consistency of the long-time averages with those computed using (11) is evidence of ergodicity for this chaotic set.

In summary, we have shown that periodic orbits can be utilized for producing a quantitatively accurate low-dimensional model of a turbulent flow. In this study, we followed a hybrid approach and combined ideas from the dynamical systems theory with topological data analysis to produce a turbulence model with transition rules inferred from the data. In the future we plan to compute approximations to the unstable manifolds of these periodic orbits using the techniques that were introduced in ref. [37]. We expect these computations to reveal insights into dynamical connections between the periodic orbits which then could be compared to our data-driven transition rules. Finally, we would like to note the novel turbulence control paradigms suggested by our model. For example, one can imagine identifying periodic orbits with high dissipation and developing control methods to avoid them. Conversely, if a particular periodic orbit's dynamics is desirable for applications, it might be possible to stabilize it using delayed feedback [38] or related methods. In conclusion, we believe that modeling turbulence using periodic orbits not only deepens our understanding of it but also opens new avenues for applications.

The numerical calculations of this paper were performed at TUBITAK ULAKBIM High Performance and Grid Computing Center and IST Austria High Performance Computing cluster.

- 
- [1] M. Nagata, *J. Fluid Mech.* **217**, 519 (1990).
- [2] F. Waleffe, *Phys. Rev. Lett.* **81**, 4140 (1998).
- [3] G. Kawahara and S. Kida, *J. Fluid Mech.* **449**, 291 (2001).
- [4] H. Faisst and B. Eckhardt, *Phys. Rev. Lett.* **91**, 224502 (2003).
- [5] H. Wedin and R. R. Kerswell, *J. Fluid Mech.* **508**, 333 (2004).
- [6] B. Hof, C. W. H. van Doorne, J. Westerweel, F. T. M. Nieuwstadt, H. Faisst, B. Eckhardt, H. Wedin, R. R. Kerswell, and F. Waleffe, *Science* **305**, 1594 (2004).
- [7] J. F. Gibson, J. Halcrow, and P. Cvitanović, *J. Fluid Mech.* **611**, 107 (2008), [arXiv:0705.3957](https://arxiv.org/abs/0705.3957).
- [8] P. Cvitanović and J. F. Gibson, *Phys. Scr.* **T142**, 014007 (2010).
- [9] L. van Veen and G. Kawahara, *Phys. Rev. Lett.* **107**, 114501 (2011).
- [10] N. B. Budanur, K. Y. Short, M. Farazmand, A. P. Willis, and P. Cvitanović, *J. Fluid Mech.* **833**, 274 (2017), [arXiv:1705.03720](https://arxiv.org/abs/1705.03720).
- [11] N. B. Budanur, A. S. Dogra, and B. Hof, *Phys. Rev. Fluids* **4**, 102401 (2019).
- [12] E. Hopf, *Commun. Pure Appl. Math.* **1**, 303 (1948).
- [13] N. B. Budanur and B. Hof, *Phys. Rev. Fluids* **3**, 054401 (2018), [arXiv:1802.01918](https://arxiv.org/abs/1802.01918).
- [14] D. Auerbach, P. Cvitanović, J.-P. Eckmann, G. Gunaratne, and I. Procaccia, *Phys. Rev. Lett.* **58**, 23 (1987).
- [15] D. Viswanath, *J. Fluid Mech.* **580**, 339 (2007), [arXiv:physics/0604062](https://arxiv.org/abs/physics/0604062).
- [16] J. V. Shebalin and S. L. Woodruff, *Phys. Fluids* **9**, 164 (1997).
- [17] G. Yalnız and N. B. Budanur, *Chaos* **30**, 033109 (2020), [arXiv:1910.04584](https://arxiv.org/abs/1910.04584).
- [18] P. Gaspard, *Chaos, Scattering and Statistical Mechanics* (Cambridge Univ. Press, Cambridge, 1997).
- [19] P. Cvitanović, R. Artuso, R. Mainieri, G. Tanner, and G. Vattay, *Chaos: Classical and Quantum* (Niels Bohr Inst., Copenhagen, 2017) *webbook*, *stable version 15.9*, [ChaosBook.org](https://chaosbook.org).
- [20] Y. Lai and T. Tél, *Transient Chaos: Complex Dynamics on Finite Time Scales* (Springer, New York, 2011).
- [21] L. van Veen and S. Goto, *Fluid Dyn. Res.* **48**, 061425 (2016).
- [22] P. Manneville, *Mech. Eng. Rev.* **3**, 15 (2016).
- [23] S. A. Orszag, *Phys. Fluids* **12**, II (1969).
- [24] C. Canuto, M. Y. Hussaini, A. Quarteroni, and T. A. Zang, *Spectral Methods: Evolution to Complex Geometries and Applications to Fluid Dynamics* (Springer, New York, 2007).
- [25] S. G. Chumakov, *Phys. Fluids* **19**, 058104 (2007).
- [26] A. P. Willis, *SoftwareX* **6**, 124 (2017).
- [27] N. Saul and C. Tralie, “Scikit-tda: Topological data analysis for python,” (2019).
- [28] N. B. Budanur, P. Cvitanović, R. L. Davidchack, and E. Siminos, *Phys. Rev. Lett.* **114**, 084102 (2015), [arXiv:1405.1096](https://arxiv.org/abs/1405.1096).
- [29] N. B. Budanur and P. Cvitanović, *J. Stat. Phys.* **167**, 636 (2017), [arXiv:1509.08133](https://arxiv.org/abs/1509.08133).
- [30] G. Yalnız and N. B. Budanur, “dnsbox code & data, [github.com/burakbudanur/dnsbox](https://github.com/burakbudanur/dnsbox),” (2020), Periodic orbit data along with our DNS code will be available in this repository.
- [31] I. T. Jolliffe, *Principal Component Analysis, Second Edition* (Springer, 2002).
- [32] H. Edelsbrunner and J. Harer, “Persistent homology—a survey,” in *Goodman JE, Pach J, Pollack R (eds) Surveys on discrete and computational geometry: twenty years later. Contemporary mathematics, vol 453*. (Am. Math. Soc., Providence, 2008) pp. 257–282.
- [33] C. Epstein, G. Carlsson, and H. Edelsbrunner, *Inverse Probl.* **27**, 120201 (2011).
- [34] N. Otter, M. A. Porter, U. Tillmann, P. Grindrod, and H. A. Harrington, *EPJ Data Sci* **6**, 17 (2017), [arXiv:1506.08903](https://arxiv.org/abs/1506.08903).
- [35] In general, higher-dimensional voids are included in persistence diagrams, however, in our applications we consider one-dimensional holes only.
- [36] A. Papoulis and S. U. Pillai, *Probability, Random Variables, and Stochastic Processes* (McGraw-Hill, 2002).
- [37] N. B. Budanur and B. Hof, *J. Fluid Mech.* **827**, R1 (2017), [10.1017/jfm.2017.516](https://doi.org/10.1017/jfm.2017.516), [arXiv:1703.10484](https://arxiv.org/abs/1703.10484).
- [38] K. Pyragas, *Phys. Lett. A* **170**, 421 (1992).